X-Nuclei MRI on a 7T MAGNETOM Terra: Initial Experiences

Tobias Wilferth[1]; Lena V. Gast[1,2]; Sebastian Lachner[1]; Nicolas G. R. Behl[3]; Manuel Schmidt[4]; Arnd Dörfler[4]; Michael Uder[1]; Armin M. Nagel[1,2,5]

[1]Institute of Radiology, University Hospital Erlangen, Friedrich-Alexander-Universität Erlangen-Nürnberg (FAU), Erlangen, Germany
[2]Institute of Medical Physics, Friedrich-Alexander-Universität Erlangen-Nürnberg (FAU), Erlangen, Germany
[3]Siemens Healthcare GmbH, Erlangen, Germany
[4]Department of Neuroradiology, University Hospital Erlangen, Friedrich-Alexander-Universität Erlangen-Nürnberg (FAU), Erlangen, Germany
[5]Division of Medical Physics in Radiology, German Cancer Research Center (DKFZ), Heidelberg, Germany

Introduction

Ions such as sodium (Na^+), potassium (K^+) and chlorine (Cl^-) play a vital role in many cellular processes. Healthy tissue contains very little extracellular K^+ ($[K^+]_e$ = 2.5–3.5 mM) but a large amount of intracellular K^+ ($[K^+]_i$ = 140 mM). The Na^+ gradient is reversed and a little less pronounced ($[Na^+]_i$ = 10–15 mM; $[Na^+]_e$ = 145 mM). Cl^- is the most abundant anion in the human body.

Cellular exchange processes, such as the Na^+/K^+-ATPase pump [1] maintain chemical and electrical gradients across the cell membrane – essential for regulating cell volume, energy production and consumption, as well as excitation of muscle or neuronal cells. Independent of its origin, loss of ATPase function leads to breakdown of the resting transmembrane potential difference, and finally to cell death as well as increase of the extracellular volume fraction.

As a result, changes in ion homeostasis can be early markers for many disease processes [2], and MRI can reveal such changes non-invasively. Nuclei other than ^1H are denoted X-nuclei and among them sodium (^{23}Na) provides the best properties for *in vivo* MRI. ^{23}Na MRI has been performed since the 1980s, even at low field strengths [3], and it is established as a non-invasive technique in clinical research [4, 5]. Numerous studies on sodium MRI have promised new metabolic information for many diseases such as stroke [6, 7], tumors [8], and multiple sclerosis [9, 10], epilepsy [11], osteoarthritis [12], diabetes [13], hypertension [14], muscular dystrophies [15], and muscular channelopathies [16].

However, X-nuclei imaging is challenging for several reasons. First of all, the signal-to-noise ratio (SNR) is several orders of magnitude lower compared to proton (^1H) MRI. In most situations relevant for human imaging, noise is dominated by the sample. And for low frequencies, which is usually the case for X-nuclei MRI, a linear noise model can be assumed. In this case, the SNR depends on the concentration c, the magnetic spin moment I and the gyromagnetic ratio γ of the nucleus as given in Equation 1 [17]:

Equation 1
$$SNR \propto c \cdot I\,(\,I+1\,) \cdot \gamma^2$$

Due to the intrinsically reduced NMR sensitivity, which results from the lower gyromagnetic ratio and the low *in vivo* concentrations of X-nuclei, compared to ^1H, their SNR is considerably lower (see Table 1). To achieve sufficient SNR for imaging, large voxel volumes are required. In addition, long acquisition times and ultra-high magnetic field strengths ($B_0 \geq$ 7T) both increase SNR.

Depending on the noise model, the SNR shows at least a linear increase with the main magnetic field strength B_0 [17] (see Figure 1A-C). MRI at field strengths of 7 Tesla and above enable imaging of nuclei such as ^{35}Cl and ^{39}K that have even lower SNR than ^{23}Na (see Table 1). Due to its low SNR, ^{39}K MRI was not considered to be practical in a clinical setting for many years [24]. This changed with the advent of ultra-high field (UHF) MR systems, and the feasibility of

[35]Cl and [39]K MRI has been shown using 7T and 9.4T UHF systems [22, 23, 25]. Even the feasibility of cardiac [39]K MRI has now been demonstrated [26]. As an investigation of the *in vivo* ion homeostasis in healthy and pathological tissue by non-invasive MRI quantification is of high medical interest, further advancements of these methods are highly desirable. For this purpose, UHF systems with approval as a medical device such as MAGNETOM Terra, which first entered the market in 2017, are of great importance.

Furthermore, X-nuclei with a spin $I > 1/2$ (e.g., [23]Na, [39]K) generally experience very rapid relaxation. Therefore, acquisition techniques enabling ultra-short echo times such as density-adapted projection reconstruction [27] or twisted projection imaging [28] are essential for efficient imaging of fast relaxing nuclei [29].

Sodium MRI using a 32-channel phased array head coil

The following measurements were performed with a MAGNETOM Terra 7T MR system (Siemens Healthcare, Erlangen, Germany) using a dual tuned proton/sodium (^{1}H/[23]Na) birdcage head coil (RAPID Biomedical, Rimpar, Germany) with 32 additionally integrated receive-only elements for [23]Na MRI. All [23]Na images were acquired using a density adapted 3D radial projection pulse sequence [27] (TR/TE = 120 ms/0.3 ms, FA = 90°, T_{RO} = 9.98 ms, T_{AQ} = 14:00 min, (2.5 mm)^3 nominal isotropic resolution).

In addition to providing higher static magnetic fields, phased array coils can further increase SNR compared with volume coils (see Figure 1C, D and Figure 2A, B) because they consist of many small receiver elements [30–32].

1A	1B	1C	1D
1.5T	3T	7T (birdcage)	7T (phased array)
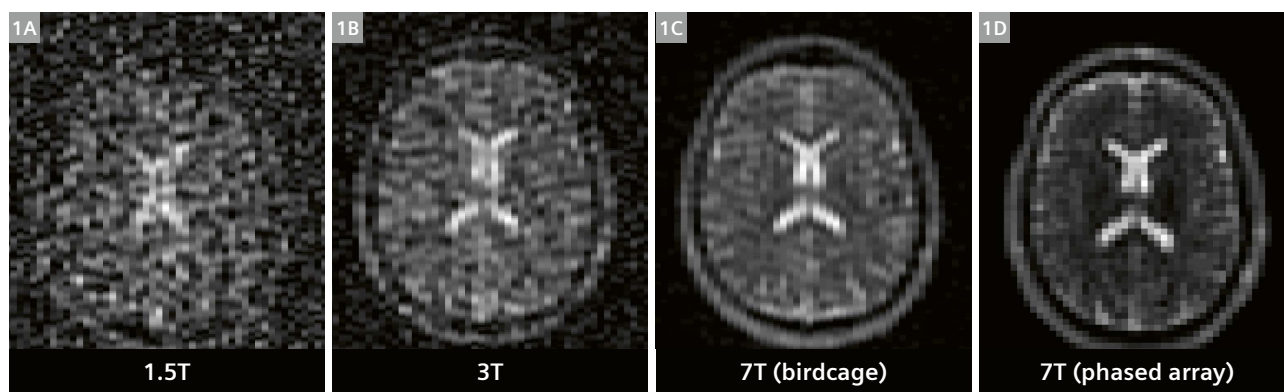
1 [23]Na MR brain images acquired at 1.5T **(1A)**, 3T **(1B)** and 7T **(1C, D)** using a density adapted 3D radial projection pulse sequence. At 7T, one image was acquired using a birdcage volume coil **(1C)** and one image using a 32-channel phased array coil **(1D)**. All data sets have a nominal isotropic resolution of (4 mm)^3. The SNR increases with magnetic field strength and the phased array coil yields higher SNR than the birdcage coil. Parameters: TE (1.5T and 3T) = 0.2 ms, TE (7T) = 0.5 ms, TR = 50 ms, FA = 77°, T_{RO} = 5 ms, T_{AQ} = 10:50 min.

Nucleus	Spin I	Natural Abundance [%]	Typical *in vivo* concentrations c [mol/L]	γ/2π [MHz/T]	Relative *in vivo* SNR[a] [%]
[1]**H**	1/2	99.99	79[b]	42.58	100
[23]**Na**	3/2	100	0.041 / 0.3[c]	11.27	$1.8 \cdot 10^{-2}$ / $1.3 \cdot 10^{-1}$
[35]**Cl**	3/2	75.78	0.027[d]	4.18	$2.2 \cdot 10^{-3}$
[39]**K**	3/2	93	0.108[e]	1.99	$1.6 \cdot 10^{-3}$

Table 1: Physical properties of selected X-nuclei and ^{1}H for comparison [17, 18].
[a]SNR values derived from Equation [1]
[b]Derived from measured water content (71%) of brain white matter [19]
[c]Measured [23]Na concentration of healthy brain white matter [20] and healthy articular cartilage [21]
(highest [23]Na content among all tissues)
[d]Measured [35]Cl concentration of healthy brain white matter [22]
[e]Measured [39]K concentration of skeletal muscle tissue [23]

However, phased array coils are only rarely used in ^{23}Na MRI, most likely due to the more complex coil design and the need to correct for the receive profile enabling ^{23}Na quantification. The latter can be addressed by optimized intensity correction methods [33].

The signal measured using the phased array coil is corrected with the receive profile of the phased array coil to obtain the real magnetization of the object. In order to determine the receive profile, a homogeneous reference image is acquired, for example via the integrated birdcage coil. A 3D sensitivity map can be obtained by dividing the low-pass filtered phased array image (which may be reconstructed via adaptive combination reconstruction [34, 35]) by the low-pass filtered reference image. Under the assumption of negligible noise, dividing the phased array image by the sensitivity map yields the intensity corrected image.

As the correction via a birdcage reference image requires additional acquisition time, a different approach using a universal sensitivity map has been evaluated [33]. The universal sensitivity map was determined by averaging individually calculated receive profiles of eight volunteers, obtained following the procedure described above.

Both approaches were applied to correct the receive profile of ^{23}Na *in vivo* measurements of the human brain, and validated by calculating of an averaged signal intensity ratio between the outer and inner CSF compartment (CSF_{out}:CSF_{in}) after performing a partial volume correction [20]. Both methods correct the intensity of the lateral ventricles in the center of the brain, which is most affected by the inhomogeneous receive profile (see Figure 3 for example data on one volunteer). No remaining intensity modulations are apparent in the ratios between the homogeneous birdcage image and the corrected phased array images. Furthermore, the signal intensities for the outer and inner CSF compartment converge. Averaged over the results of eight examined subjects, the ratio CSF_{out}:CSF_{in}
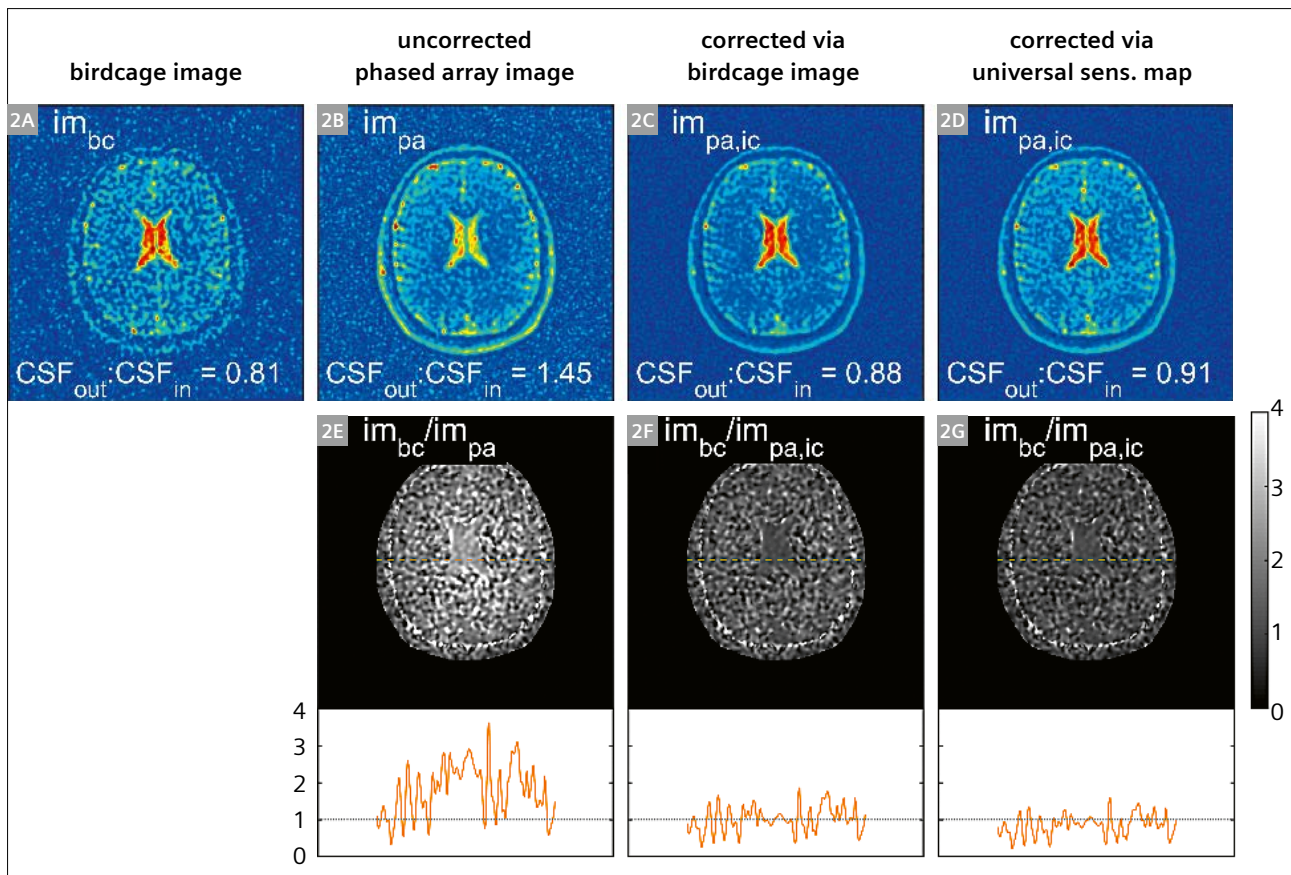
2 Representative intensity correction of a measured ^{23}Na MRI in vivo data, using a birdcage image **(2C)** and a universal sensitivity map **(2D)**. The ratio between the uncorrected phased array image **(2B)** and the birdcage image **(2A)** indicates an intensity modulation due to the inhomogeneous receive profile **(2E)**. For the corrected phased array images **(2C, D)** the ratios **(2F, G)** indicate a good performance of the applied correction methods.

for the uncorrected phased array image is 1.71 due to underestimation of the signal intensity in the center of the brain. For the birdcage image the averaged ratio is 0.89. After applying the intensity correction using a birdcage image, an averaged ratio of 1.00 is obtained. Using the universal sensitivity map instead of the individual birdcage image results in an averaged ratio of 1.05 [33].

So the method utilizing a birdcage image performs better but requires considerably longer acquisition time [33], while the universal sensitivity map performs only slightly worse. As there only seems to be a small subject dependency of the coil sensitivities, even a low number of averaged *in vivo* datasets should be sufficient to determine the universal sensitivity map (here n = 8).

Figure 3 shows an intensity-corrected ^{23}Na MRI dataset (using the universal sensitivity map) of a glioblastoma patient. The intensity of the right lateral ventricle in the center of the brain is increased in the corrected phased array image as compared to the uncorrected phased array image, and comparable to the intensity in the outer CSF compartment (see Figure 3A). In Figure 3B concentration

maps of different slices are shown. The concentration values were normalized to 145 mM in the CSF of the ventricles, which were used as internal reference.

Iterative reconstruction

As mentioned above, the low SNR of ^{23}Na MRI results in low spatial resolution and long acquisition time. One way to counteract this is Compressed Sensing (CS) image reconstruction. The 3D radial trajectory used for ^{23}Na MRI is well suited for CS, since resulting undersampling artifacts appear noise-like. On the other hand, the inherent low SNR in the data is not ideal for CS approaches. One way to get the most out of ^{23}Na MRI reconstructions is to undersample the radial data and invest the time gained into averaging [36]. Figure 4 shows the standard reconstruction (NUFFT) and the Dictionary Learning CS reconstruction (3D-DLCS) of ^{23}Na MRI volunteer data, with a nominal resolution of 2 mm isotropic. The data are 10-fold undersampled and 10-fold averaged.
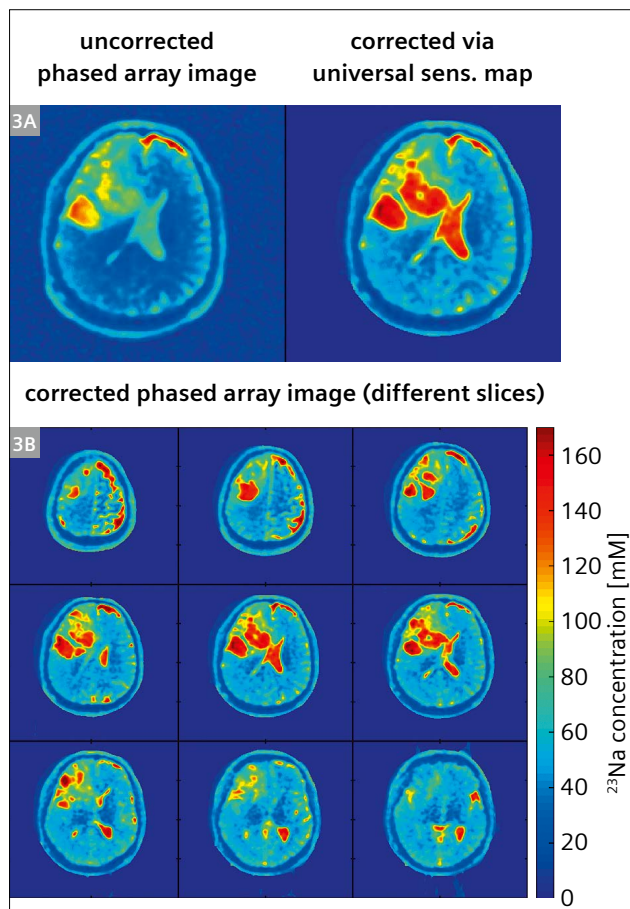
3 ^{23}Na MRI of a glioblastoma patient using a 32-channel phased array head coil and intensity correction via a universal sensitivity map (spatial resolution: isotropic (2.5 mm)^3, T_{AQ} = 14:00 min). The region of the tumor shows higher sodium concentration.
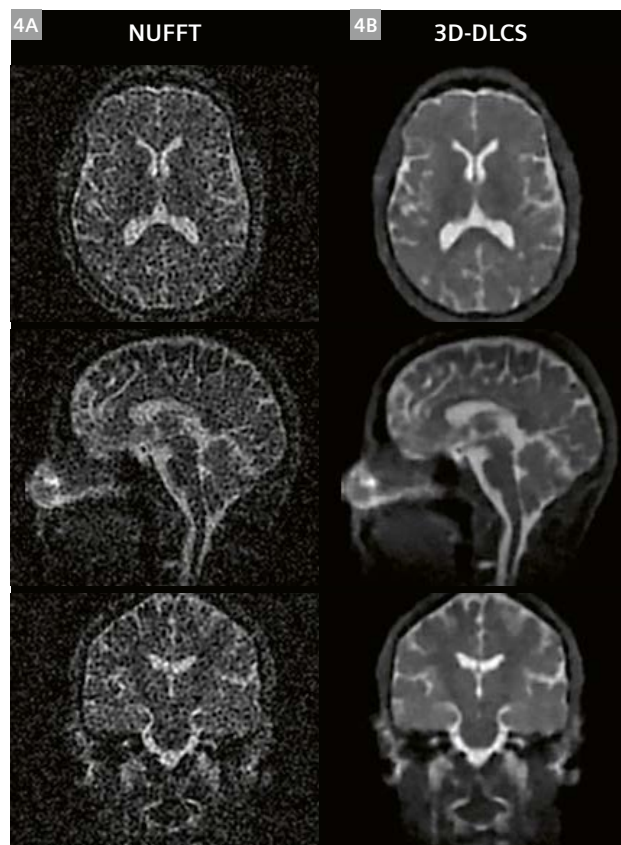
4 Reconstructions of 10-fold undersampled and 10-fold averaged ^{23}Na MRI data with a nominal resolution of 2 mm isotropic. While the NUFFT reconstruction **(4A)** displays strong noise contamination, image noise is markedly reduced in the 3D-DLCS reconstruction **(4B)**.

Combined ^{23}Na/^{39}K MRI of human skeletal muscle

Due to the inverse Na$^+$ and K$^+$ ion distribution between the intracellular and extracellular spaces, a combined determination of their tissue concentrations using ^{23}Na and ^{39}K MRI might give interesting insights into the physiology. While alterations in tissue sodium content (TSC) have been examined in various diseases using ^{23}Na MRI [14, 15, 37–39], in clinical practice, K$^+$ concentrations are currently only determined using extracellular body fluids such as blood samples. However, changes in total K$^+$ content in the human body are mainly buffered in the intracellular space [40], so a direct detection of tissue potassium content (TPC) using ^{39}K MRI might be beneficial.

For combined ^{23}Na/^{39}K MRI, we used a dual tuned, circular polarized ^{23}Na/^{39}K calf coil[1] with inner diameter of 20 cm (Rapid Biomedical, Rimpar, Germany). With this coil, imaging of both nuclei can be realized without repositioning the leg. However, no ^{1}H channel is included for the acquisition of anatomical images. Moreover, B$_0$ shimming in X-nuclei imaging is usually performed using the ^{1}H channel of a dual tuned (e.g., ^{23}Na/^{1}H) coil, or using a ^{1}H body coil. If no ^{1}H channel is available, B$_0$ shimming cannot be performed using vendor-provided B$_0$ shimming techniques as they are generally based on B$_0$ maps acquired by ^{1}H MRI. As a homogeneous B$_0$ field is indispensable, especially for quantitative measurements [41], a custom B$_0$ shimming routine based on ^{23}Na MRI data was implemented [42]. To verify this shimming approach, we compared its performance with conventional vendor-provided ^{1}H MRI based B$_0$ shimming routines, and used the double resonant 32-channel ^{23}Na/^{1}H head coil (Rapid Biomedical, Rimpar, Germany) described above.

^{23}Na B$_0$ maps are acquired using a double-echo 3D density-adapted radial readout (DA-3D-RAD) scheme [27]. Shim values are calculated using the constrained regularized pseudo-inversion approach (ConsTru) proposed by Nassirpour et al. [43]. The volume of interest to be shimmed is defined by a three-dimensional mask calculated by thresholding based on the magnitude image corresponding to the first echo. Reconstruction and post-processing of the radial datasets, as well as shim value calculation, are performed on the host computer of the MR system using MATLAB (TheMathworks, Natick, MA, USA).

B$_0$ shimming of the human head was performed both based on ^{23}Na MRI and using the vendor-provided ^{1}H MRI based GRE Brain shimming routine. For better comparability, only one iteration of shimming was performed each for the ConsTru and the GRE Brain shim in all measurements. Additionally, the acquisition duration of the ^{23}Na images used for the shim value calculation was chosen to match
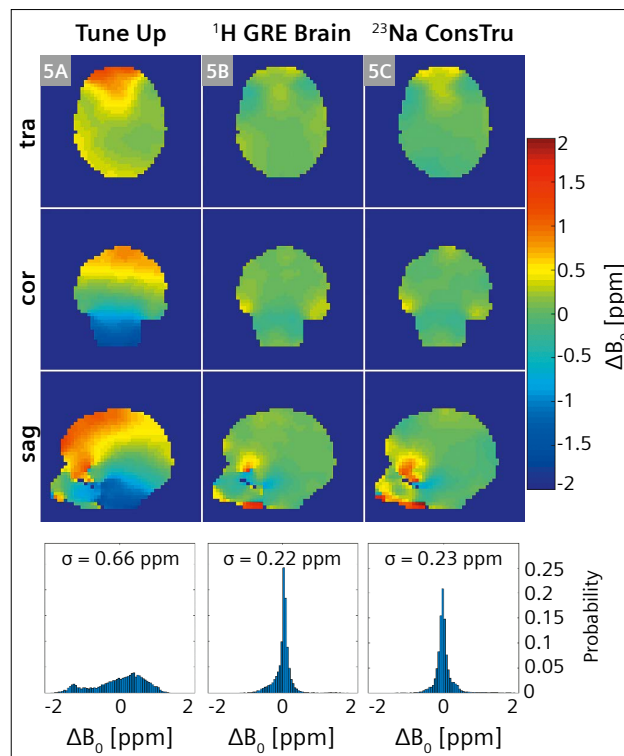
5 B$_0$ homogeneity in the human brain using: system default shim settings (denoted as Tune Up shim settings) **(5A)**, shim values calculated by the vendor-provided ^{1}H GRE Brain shim **(5B)** implemented ^{23}Na MRI based ConsTru shim **(5C)**. The last two routines show similar resulting B$_0$ homogeneity with a reduction of the B$_0$ variations over the entire volume of interest by 67% (GRE Brain shim) and 65% (^{23}Na ConsTru). Similar data can be found in Gast et al. [42].

the acquisition duration of the GRE Brain shimming B$_0$ map acquisition (N$_{proj}$ = 300). The resulting B$_0$ homogeneity is shown in Figure 5. Over six examined volunteers, we observed a very similar performance of both shimming routines with a mean reduction of the B$_0$ variations σ by 53 ± 7% (^{1}H GRE Brain) and 52 ± 7% (^{23}Na ConsTru) over the entire head volume. Therefore, we conclude that B$_0$ shimming based on ^{23}Na MRI is feasible in clinically acceptable acquisition durations with satisfactory outcome.

For quantitative ^{23}Na and ^{39}K imaging, human lower legs are positioned on a five-compartment reference tube holder filled with different combinations of NaCl and K$_2$HPO$_4$ solution, corresponding to different Na$^+$ (10–40 mM) and K$^+$ (120–240 mM) concentrations. K$_2$HPO$_4$ solution has lower electrical conductivity than KCl solution, and is therefore expected to produce fewer image artifacts. Images are acquired using an acquisition-weighted stack-of-stars (AW-SOS) scheme [44]. Parameters (^{23}Na/^{39}K): TR = 120/40 ms, TE = 0.3/0.4 ms, T$_{RO}$ = 10/5 ms, FA = 90°, rectangular excitation pulse of 500 ms duration,

---

[1]The information shown herein refers to products of 3rd party manufacturer's and thus are in their regulatory responsibility. Please contact the 3rd party manufacturer for further information.
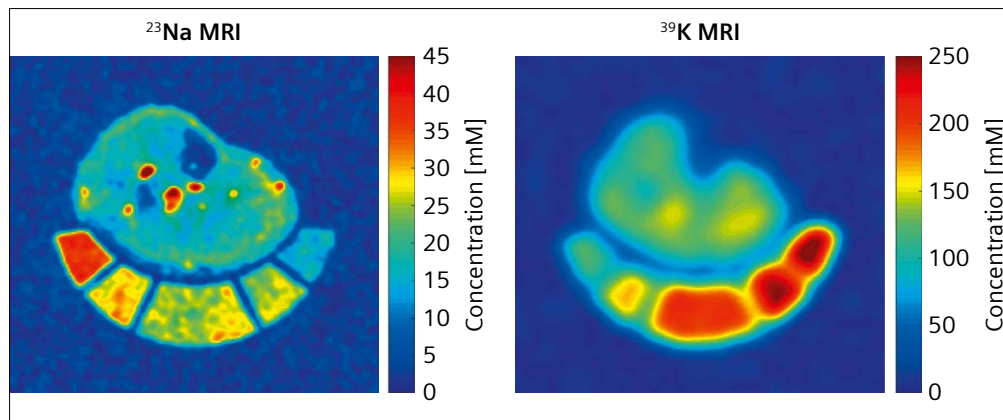
6 Exemplary ^{23}Na and ^{39}K concentration maps of healthy human lower leg calculated from ^{23}Na and ^{39}K MRI datasets. Concentration calibration was performed by a linear regression, based on the signal intensity within the reference compartments containing NaCl and K_2HPO_4 solution.

nominal spatial resolution $\Delta x = 2.5 \times 2.5 \times 10$ mm^3 / $7.5 \times 7.5 \times 30$ mm^3, averages = 1/4, total acquisition time $T_{AQ} = 10:54 / 8:06$ min.

Concentration calibration is performed by linear regression of the ^{23}Na and ^{39}K signal intensities within the reference compartments to their nominal concentrations. Resulting ^{23}Na and ^{39}K concentration maps of healthy lower leg are shown in Figure 6. However, for precise quantification of Na$^+$ and K$^+$ concentrations based on ^{23}Na and ^{39}K images, several signal corrections are required. For ^{39}K especially, low image resolution leads to a strong partial volume effect. Moreover, muscle tissue has significantly shorter T2* and T1 relaxation times than the reference solutions both for ^{23}Na and ^{39}K, so a relaxation correction is needed.

So far, ^{39}K concentration maps have been acquired only for healthy muscle tissue. However, examining potassium concentrations would be of interest in various diseases, for example renal impairment and muscular diseases, to help reveal underlying physiological processes.

Conclusion

Introducing clinically approved UHF scanners such as MAGNETOM Terra, together with suitable RF coils and sequences, was an important step for X-nuclei imaging, which benefits from the increased SNR and resultant higher spatial resolution or shorter acquisition time. This paves the way for ^{23}Na MRI to move from research into clinical applications. Tissue sodium concentration might evolve into a useful biomarker for a large variety of diseases such as kidney diseases [45], muscular diseases [46], and neurodegeneration [9]. Moreover, MRI of other nuclei such as ^{39}K becomes possible in a clinical environment with feasible measurement times. Compared with morphological ^{1}H MRI, these nuclei provide additional information that will provide insights into many physiologically relevant processes, resulting in various potential clinical research applications.

References

1 Robinson JD, Flashner MS. The (Na+ + K+)-activated ATPase. Enzymatic and transport properties. Biochim Biophys Acta 1979;549(2):145-176.

2 Rose AM, Valdes R, Jr. Understanding the sodium pump and its relevance to disease. Clin Chem 1994;40(9):1674-1685.

3 Hilal SK, Maudsley AA, Ra JB, Simon HE, Roschmann P, Wittekoek S, Cho ZH, Mun SK. In vivo NMR imaging of sodium-23 in the human head. J Comput Assist Tomogr 1985;9(1):1-7.

4 Madelin G, Regatte RR. Biomedical applications of sodium MRI in vivo. J Magn Reson Imaging 2013;38(3):511-529.

5 Thulborn KR. Quantitative sodium MR imaging: A review of its evolving role in medicine. Neuroimage 2018;168:250-268.

6 Thulborn KR, Gindin TS, Davis D, Erb P. Comprehensive MR imaging protocol for stroke management: tissue sodium concentration as a measure of tissue viability in nonhuman primate studies and in clinical studies. Radiology 1999;213(1):156-166.

7 Hussain MS, Stobbe RW, Bhagat YA, Emery D, Butcher KS, Manawadu D, Rizvi N, Maheshwari P, Scozzafava J, Shuaib A, Beaulieu C. Sodium imaging intensity increases with time after human ischemic stroke. Ann Neurol 2009;66(1):55-62.

8 Schepkin VD. Sodium MRI of glioma in animal models at ultrahigh magnetic fields. NMR Biomed 2016;29(2):175-186.

9 Huhn K, Engelhorn T, Linker RA, Nagel AM. Potential of Sodium MRI as a Biomarker for Neurodegeneration and Neuroinflammation in Multiple Sclerosis. Front Neurol 2019;10:84.

10 Petracca M, Fleysher L, Oesingmann N, Inglese M. Sodium MRI of multiple sclerosis. NMR Biomed 2016;29(2):153-161.

11 Ridley B, Marchi A, Wirsich J, Soulier E, Confort-Gouny S, Schad L, Bartolomei F, Ranjeva JP, Guye M, Zaaraoui W. Brain sodium MRI in human epilepsy: Disturbances of ionic homeostasis reflect the organization of pathological regions. Neuroimage 2017;157:173-183.

12 Zbyn S, Mlynarik V, Juras V, Szomolanyi P, Trattnig S. Evaluation of cartilage repair and osteoarthritis with sodium MRI. NMR Biomed 2016;29(2):206-215.

13 Kopp C, Linz P, Maier C, Wabel P, Hammon M, Nagel AM, Rosenhauer D, Horn S, Uder M, Luft FC, Titze J, Dahlmann A. Elevated tissue sodium deposition in patients with type 2 diabetes on hemodialysis detected by ^{23}Na magnetic resonance imaging. Kidney Int 2018;93(5):1191-1197.

14 Kopp C, Linz P, Dahlmann A, Hammon M, Jantsch J, Muller DN, Schmieder RE, Cavallaro A, Eckardt KU, Uder M, Luft FC, Titze J. 23Na magnetic resonance imaging-determined tissue sodium in healthy subjects and hypertensive patients. Hypertension 2013;61(3):635-640.

15 Gerhalter T, Gast LV, Marty B, Martin J, Trollmann R, Schussler S, Roemer F, Laun FB, Uder M, Schroder R, Carlier PG, Nagel AM. (23) Na MRI depicts early changes in ion homeostasis in skeletal muscle tissue of patients with duchenne muscular dystrophy. J Magn Reson Imaging 2019;50(4):1103-1113.
16 Weber MA, Nagel AM, Marschar AM, Glemser P, Jurkat-Rott K, Wolf MB, Ladd ME, Schlemmer HP, Kauczor HU, Lehmann-Horn F. 7-T Cl and Na MR Imaging for Detection of Mutation-dependent Alterations in Muscular Edema and Fat Fraction with Sodium and Chloride Concentrations in Muscular Periodic Paralyses. Radiology 2016;280(3):848-859.
17 Ladd ME, Bachert P, Meyerspeer M, Moser E, Nagel AM, Norris DG, Schmitter S, Speck O, Straub S, Zaiss M. Pros and cons of ultra-high-field MRI/MRS for human application. Prog Nucl Magn Reson Spectrosc 2018;109:1-50.
18 Harris RK, Becker ED, Cabral de Menezes SM, Goodfellow R, Granger P. NMR Nomenclature: Nuclear Spin Properties and Conventions for Chemical Shifts. IUPAC Recommendations 2001. Solid State Nucl Magn Reson 2002;22(4):458-483.
19 Neeb H, Zilles K, Shah NJ. A new method for fast quantitative mapping of absolute water content in vivo. Neuroimage 2006;31(3):1156-1168.
20 Niesporek SC, Hoffmann SH, Berger MC, Benkhedah N, Kujawa A, Bachert P, Nagel AM. Partial volume correction for in vivo (23)Na-MRI data of the human brain. Neuroimage 2015;112:353-363.
21 Madelin G, Lee JS, Regatte RR, Jerschow A. Sodium MRI: methods and applications. Prog Nucl Magn Reson Spectrosc 2014;79:14-47.
22 Nagel AM, Lehmann-Horn F, Weber MA, Jurkat-Rott K, Wolf MB, Radbruch A, Umathum R, Semmler W. In vivo 35Cl MR imaging in humans: a feasibility study. Radiology 2014;271(2):585-595.
23 Umathum R, Rosler MB, Nagel AM. In vivo 39K MR imaging of human muscle and brain. Radiology 2013;269(2):569-576.
24 Parrish TB, Fieno DS, Fitzgerald SW, Judd RM. Theoretical basis for sodium and potassium MRI of the human heart at 1.5 T. Magn Reson Med 1997;38(4):653-661.
25 Atkinson IC, Claiborne TC, Thulborn KR. Feasibility of 39-potassium MR imaging of a human brain at 9.4 Tesla. Magn Reson Med 2014;71(5):1819-1825.
26 Wenz D, Nagel AM, Lott J, Kuehne A, Niesporek SC, Niendorf T. In vivo potassium MRI of the human heart. Magn Reson Med 2020;83(1):203-213.
27 Nagel AM, Laun FB, Weber MA, Matthies C, Semmler W, Schad LR. Sodium MRI using a density-adapted 3D radial acquisition technique. Magn Reson Med 2009;62(6):1565-1573.
28 Boada FE, Gillen JS, Shen GX, Chang SY, Thulborn KR. Fast three dimensional sodium imaging. Magn Reson Med 1997;37(5):706-715.
29 Konstandin S, Nagel AM. Measurement techniques for magnetic resonance imaging of fast relaxing nuclei. MAGMA 2014;27(1):5-19.
30 Roemer PB, Edelstein WA, Hayes CE, Souza SP, Mueller OM. The NMR phased array. Magn Reson Med 1990;16(2):192-225.
31 Wiggins GC, Brown R, Lakshmanan K. High-performance radiofrequency coils for (23)Na MRI: brain and musculoskeletal applications. NMR Biomed 2016;29(2):96-106.
32 Bangerter NK, Kaggie JD, Taylor MD, Hadley JR. Sodium MRI radiofrequency coils for body imaging. NMR Biomed 2016;29(2):107-118.
33 Lachner S, Ruck L, Niesporek SC, Utzschneider M, Lott J, Hensel B, Dorfler A, Uder M, Nagel AM. Comparison of optimized intensity correction methods for (23)Na MRI of the human brain using a 32-channel phased array coil at 7 Tesla. Z Med Phys 2019; in press.

34 Benkhedah N, Hoffmann SH, Biller A, Nagel AM. Evaluation of adaptive combination of 30-channel head receive coil array data in 23Na MR imaging. Magn Reson Med 2016;75(2):527-536.
35 Walsh DO, Gmitro AF, Marcellin MW. Adaptive reconstruction of phased array MR imagery. Magn Reson Med 2000;43(5):682-690.
36 Behl NG, Gnahm C, Bachert P, Ladd ME, Nagel AM. Three-dimensional dictionary-learning reconstruction of (23)Na MRI data. Magn Reson Med 2016;75(4):1605-1616.
37 Weber MA, Nagel AM, Jurkat-Rott K, Lehmann-Horn F. Sodium (23Na) MRI detects elevated muscular sodium concentration in Duchenne muscular dystrophy. Neurology 2011;77(23):2017-2024.
38 Nagel AM, Amarteifio E, Lehmann-Horn F, Jurkat-Rott K, Semmler W, Schad LR, Weber MA. 3 Tesla sodium inversion recovery magnetic resonance imaging allows for improved visualization of intracellular sodium content changes in muscular channelopathies. Invest Radiol 2011;46(12):759-766.
39 Hammon M, Grossmann S, Linz P, Seuss H, Hammon R, Rosenhauer D, Janka R, Cavallaro A, Luft FC, Titze J, Uder M, Dahlmann A. 3 Tesla (23)Na Magnetic Resonance Imaging During Acute Kidney Injury. Acad Radiol 2017;24(9):1086-1093.
40 Palmer BF. Regulation of Potassium Homeostasis. Clin J Am Soc Nephrol 2015;10(6):1050-1060.
41 Lu A, Atkinson IC, Claiborne TC, Damen FC, Thulborn KR. Quantitative sodium imaging with a flexible twisted projection pulse sequence. Magn Reson Med 2010;63(6):1583-1593.
42 Gast LV, Henning A, Hensel B, Uder M, Nagel AM. Localized B0 shimming based on (23) Na MRI at 7 T. Magn Reson Med 2020;83(4):1339-1347.
43 Nassirpour S, Chang P, Fillmer A, Henning A. A comparison of optimization algorithms for localized in vivo B0 shimming. Magn Reson Med 2018;79(2):1145-1156.
44 Müller M, Gast LV, Hensel B, Uder M, Nagel AM. Comparison of anisotropic UTE sequences for 23Na/39K imaging in the human calf at 7T. Proc Intl Soc Mag Reson Med 27 2019.
45 Dahlmann A, Dorfelt K, Eicher F, Linz P, Kopp C, Mossinger I, Horn S, Buschges-Seraphin B, Wabel P, Hammon M, Cavallaro A, Eckardt KU, Kotanko P, Levin NW, Johannes B, Uder M, Luft FC, Muller DN, Titze JM. Magnetic resonance-determined sodium removal from tissue stores in hemodialysis patients. Kidney Int 2015;87(2):434-441.
46 Strijkers GJ, Araujo ECA, Azzabou N, Bendahan D, Blamire A, Burakiewicz J, Carlier PG, Damon B, Deligianni X, Froeling M, Heerschap A, Hollingsworth KG, Hooijmans MT, Karampinos DC, Loudos G, Madelin G, Marty B, Nagel AM, Nederveen AJ, Nelissen JL, Santini F, Scheidegger O, Schick F, Sinclair C, Sinkus R, de Sousa PL, Straub V, Walter G, Kan HE. Exploration of New Contrasts, Targets, and MR Imaging and Spectroscopy Techniques for Neuromuscular Disease – A Workshop Report of Working Group 3 of the Biomedicine and Molecular Biosciences COST Action BM1304 MYO-MRI. J Neuromuscul Dis 2019;6(1):1-30.

Contact

Professor Armin Nagel
Institute of Radiology
University Hospital Erlangen
Maximiliansplatz 3
91054 Erlangen
Germany
Tel.: +49 (0)9131 85-25900
armin.nagel@uk-erlangen.de